

Cold-Adaptation Signatures in the Ligand Rebinding Kinetics to the Truncated Hemoglobin of the Antarctic Bacterium *Pseudoalteromonas haloplanktis* TAC125

Fernando M. Boubeta,[†] Leonardo Boechi,[‡] Dario Estrin,[†] Barbara Patrizi,^{§,||} Mariangela Di Donato,^{§,||} Alessandro Iagatti,[§] Daniela Giordano,^{⊥,#} Cinzia Verde,^{⊥,#} Stefano Bruno,[∇] Stefania Abbruzzetti,[○] and Cristiano Viappiani^{*,○}

[†]Instituto de Química Física de los Materiales, Medio Ambiente y Energía (INQUIMAE), CONICET, and Universidad de Buenos Aires, C1428EHA Buenos Aires, Argentina

[‡]Instituto de Calculo, Facultad de Ciencias Exactas y Naturales, Universidad de Buenos Aires, C1428EGA Buenos Aires, Argentina

[§]European Laboratory for Non Linear Spectroscopy (LENS), Università di Firenze, Via Nello Carrara 1, 50019 Sesto Fiorentino, Florence, Italy

^{||}INO-CNR, Istituto Nazionale di Ottica, Consiglio Nazionale delle Ricerche, Largo Fermi 6, 50125 Florence, Italy

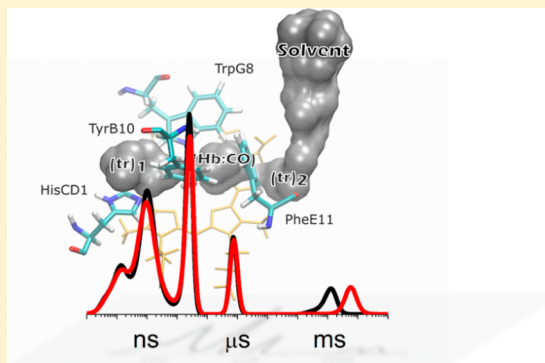
[⊥]Institute of Biosciences and BioResources (IBBR), CNR, Via Pietro Castellino 111, I-80131 Naples, Italy

[#]Stazione Zoologica Anton Dohrn, Villa Comunale, 80121 Naples, Italy

[∇]Dipartimento di Scienze degli Alimenti e del Farmaco, Università di Parma, Parco Area delle Scienze 23A, 43124, Parma, Italy

[○]Dipartimento di Scienze Matematiche, Fisiche e Informatiche, Università di Parma, Parco Area delle Scienze 7A, 43124, Parma, Italy

ABSTRACT: Cold-adapted organisms have evolved proteins endowed with higher flexibility and lower stability in comparison to their thermophilic homologues, resulting in enhanced reaction rates at low temperatures. In this context, protein-bound water molecules were suggested to play a major role, and their weaker interactions at protein active sites have been associated with cold adaptation. In this work, we tested this hypothesis on truncated hemoglobins (a family of microbial heme-proteins of yet-unclear function) applying molecular dynamics simulations and ligand-rebinding kinetics on a protein from the Antarctic bacterium *Pseudoalteromonas haloplanktis* TAC125 in comparison with its thermophilic *Thermobifida fusca* homologue. The CO rebinding kinetics of the former highlight several geminate phases, with an unusually long-lived geminate intermediate. An articulated tunnel with at least two distinct docking sites was identified by analysis of molecular dynamics simulations and was suggested to be at the origin of the unusual geminate rebinding phase. Water molecules are present in the distal pocket, but their stabilization by TrpG8, TyrB10, and HisCD1 is much weaker than in thermophilic *Thermobifida fusca* truncated hemoglobin, resulting in a faster geminate rebinding. Our results support the hypothesis that weaker water-molecule interactions at the reaction site are associated with cold adaptation.



INTRODUCTION

The ability of organisms to survive to extreme temperatures relies on the adaptation of their proteins to work under these conditions. Particularly, it is generally accepted that cold-adapted organisms have evolved proteins with structural and dynamical features conferring higher flexibility and lower stability in comparison to their thermophilic counterparts, resulting in low activation enthalpies and enhanced reaction rates of the reactions they catalyze in environments with low kinetic energy.^{1,2} Solvent molecules populating inner protein cavities, especially at active sites, play a role in tuning reaction rates and were suggested to be a key factor in temperature

adaptation of proteins with similar fold and function.^{3,4} For instance, Paredes et al. have recently considered in a systematic study 20 homologous enzyme pairs from psychrophiles and mesophiles in order to characterize flexibility as a key feature of cold adaptation. They found that psychrophilic enzymes have larger average cavity sizes, large enough for water molecules, and they are lined with amino acid with acidic side chains.

Special Issue: William A. Eaton Festschrift

Received: August 7, 2018

Revised: September 18, 2018

Published: September 19, 2018

They concluded that embedded water molecules may play a significant role in cavity flexibility.⁵

Hemoglobins (Hbs) offer a good test case of evolutionary temperature adaptation because of the large number of homologues found in nature and the detailed characterization of their structure–function relationship. Their functional properties are associated with the environment of the heme group, which shapes their ligand binding properties and their reactivity.^{6–8} Despite the vast number of Hbs recently discovered in bacteria, our knowledge of their functional roles is very limited, with some Hbs putatively involved in the detoxification of reactive nitrogen and oxygen species.^{9–11} Bacteria express three related groups of truncated Hbs (trHbs), groups I (trHbN), II (trHbO), and III (trHbP).¹⁰ The group II trHb *Ph*-trHbO is expressed in the cold-adapted Antarctic bacterium *Pseudoalteromonas haloplanktis* TAC125,^{12–14} the first psychrophilic bacterium whose genome has been fully sequenced and the only one described in the literature in which genes encoding a flavoHb and three trHbs are present, a feature potentially related to the cold environments and the role of these proteins in nitrosative and oxidative stress.^{15,16} The topology in group-II trHbs is quite different from the one reported for group I. For instance, in *Mycobacterium tuberculosis* trHbN, a short tunnel connects the heme distal site to the outer solvent space at a location between the central region of the G and H helices, whereas a long tunnel extends from the heme distal cavity to a solvent access site located between the interhelical loops AB and GH.^{10,17–19}

The enhanced local flexibility of the cold-adapted *Ph*-trHbO was confirmed by comparison with other members of the globin family through molecular dynamics (MD) simulations. MD simulations showed significant conformational fluctuations localized mainly at the *Ph*-trHbO EF loop (residues 79–83) in comparison to other trHbs belonging to the same group.¹³

The analysis of *Ph*-trHbO by electron paramagnetic resonance and resonance Raman spectroscopy indicated that although the protein retains the general features of group II trHbs, it exhibits different heme ligation states, thus supporting a high conformational flexibility, possibly associated with cold adaptation.¹³ The adaptive structural properties of the cold-adapted protein and its enhanced flexibility were also demonstrated by its resistance to pressure-induced stress.²⁰

As in other trHbs, ligand rebinding to *Ph*-trHbO upon flash photolysis is affected by the presence of tunnels and cavities in the protein matrix, whose shape and accessibility are largely determined by protein dynamics. Previous investigations on *Ph*-trHbO indicated a large, temperature-dependent geminate rebinding phase, extending to the microsecond time scale, upon nanosecond flash photolysis.²⁰ The extent of absorbance change at the end of the laser pulse suggested that a substantial part of ligand geminate recombination may occur on the subnanosecond time scale.

In this work, we have investigated ligand rebinding using a combination of femtosecond transient absorbance and nanosecond laser flash photolysis to follow the full time-course of ligand rebinding, with the intent of exploring the dynamic and structural signatures of cold adaptation. The results were interpreted in view of MD simulations at different temperatures and in comparison with similar studies on thermophilic homologues.

METHODS

Protein Expression and Purification. The gene *PSHAA0030*-encoding *Ph*-trHbO was cloned, and the recombinant protein was expressed and purified as previously described.^{12,21}

Sample Preparation. The protein solutions (about 40 μM for transient absorption and 30 μM for nanosecond laser photolysis) in 20 mM Tris-HCl buffer (pH = 7.6) were equilibrated with CO at the desired pressure and reduced by adding few μL of an anaerobically prepared solution of sodium dithionite. The formation of the protein–CO adduct was checked by UV–vis spectroscopy.

Transient Absorption Spectroscopy (TAS). A full description of the apparatus is reported elsewhere.^{22–24} The output of a regenerative amplifier Ti:sapphire laser system (BMI-Alpha1000) delivering ~ 100 fs pulses at 800 nm produced both pump (second harmonic of the fundamental laser output at 400 nm, energy 0.5 μJ /pulse) and probe (white continuum) pulses. The repetition rate of the laser system was set at 100 Hz. The relative pump–probe polarization angle was set at 54.7° with the purpose of excluding rotational contributions to the transient signal. The homemade detection system consists of two linear CCD arrays (Hamamatsu S8377-256Q) coupled to a spectrograph (Jobin Yvon CP 140-1824) controlled by a homemade front-end circuit. The signals were fed into a simultaneous analog-to-digital conversion board (Adlink DAQ2010), and data were acquired by means of a LabVIEW computer program. A 2 mm thick sealed quartz cell containing the sample was mounted on a home-built scanner and moved to change the region excited by pump pulses in order to avoid sample photodegradation. The concentration (40 μM) was adjusted to yield an optical density OD ~ 1.2 at the Soret maximum, corresponding to a good signal-to-noise ratio in the whole probed spectral region. The sample was excited in resonance with the blue side of the Soret band ($\lambda_{\text{pump}} = 400$ nm, pump pulses energy 250 nJ), and the induced absorbance changes were monitored in the 400–850 nm spectral region.

The time evolution of the excited protein was monitored by measuring the change in the sample absorbance at a given delay time. By repeating this sequence as a function of the pump–probe delay, it was possible to obtain the dynamical evolution of the transient signal (up to 1.8 ns).

TAS spectra were recorded at different temperatures (0, 10, 20, 30, and 40 °C) with freshly prepared samples. The integrity of the sample was checked by UV–visible absorption after each TAS measurement.

Nanosecond Laser Photolysis. The details of the experimental setup have been reported elsewhere.²⁵ Photolysis of CO complexes was obtained using the second harmonic (532 nm) of a Q-switched Nd:YAG laser (Spectron Laser). The monochromatized (436 nm) CW output of a 150 W Xe arc lamp (AMKO GmbH) was used as probe beam, a five stages photomultiplier (Applied Photophysics) for detection, and a digital oscilloscope (LeCroy Waverunner 104-Xi, 1 GHz, 10 GS/s, 12.5 Mpts/Ch) for digitizing the voltage signal. A second monochromator (LOT-Oriel) was placed before the photomultiplier to remove the residual stray light from the pump laser. The sample holder is accurately temperature controlled with a Peltier element, allowing a temperature stability of better than 0.1 °C. Measurements were taken at 10, 20, 30, and 40 °C.

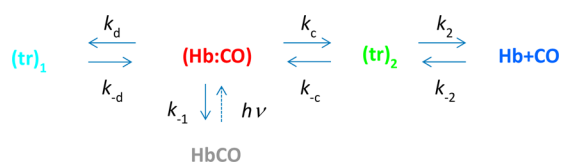
Data Analysis. TAS spectra acquired in the fs–ps time scale were analyzed by singular value decomposition (SVD),²⁶ performed using the Matlab software as previously described.²⁷ Only spectral components with correlation greater than 0.8 were kept.²⁶

The procedure for merging the kinetics measured in the two time regimes was presented in previous works.^{28,29} Essentially, absorbance change in the nanosecond photolysis experiment was normalized to the maximum absorbance change expected for full photolysis and estimated from the equilibrium spectral difference between deoxy and carboxy species at the used concentration.

Lifetime distributions associated with rebinding kinetics were determined using the program Memexp, based on a maximum entropy method,^{30,31} that proved very effective for the analysis of several rebinding kinetics to heme proteins.^{32–34}

The analysis of the entire CO rebinding kinetics required the use of a kinetic scheme sketched in Scheme 1 in order to

Scheme 1. Minimal Reaction Scheme for Ligand Rebinding Kinetics to *Ph*-trHbO^a



^aReaction scheme takes into account the presence of cavities (tr_1 and tr_2) inside the protein matrix and their topological connections with the distal cavity and the solvent phase. After photoexcitation, the photodissociated ligand is found inside the distal cavity (Hb:CO) from which it can either migrate to the off-pathway cavity (tr_1) or to the on-pathway cavity (tr_2), through which it can reach the solvent (Hb + CO in the scheme).

estimate the microscopic rate constants. The differential equations associated with the kinetic schemes were solved numerically, and the rate constants were optimized to describe simultaneously the experimental data at two different CO concentrations (1 mM and 0.2 mM, corresponding to solutions equilibrated with 1 and 0.2 atm of CO, respectively). Numerical solutions to the set of coupled differential equations associated with reaction schemes were determined by using the function ODE15s within Matlab (version 7.0, The MathWorks, Inc., Natick, MA). Fitting of the numerical solution to experimental data was obtained with a Matlab version of the optimization package Minuit (CERN). The method was discussed previously.^{29,35}

MD Simulations. The protein structure corresponding to a deoxy ferrous complex of *Ph*-trHbO was constructed from the X-ray structure file corresponding to PDB code 4UUR (trHbO from *Pseudoalteromonas haloplanktis* TAC125). Fixed protonation states of the amino acids were assumed to correspond to those at physiological pH (i.e., Asp and Glu negatively charged, Lys and Arg positively charged), and all solvent exposed His were protonated at the N- δ atom, as well as the proximal His, which is coordinated to the metal center of the heme group. The system was solvated by constructing an octahedral box of 12 Å and keeping crystallographic water molecules. Approximately 6617 TIP3P water molecules were placed inside the box through the standard criteria procedure of the AmberTools package.³⁶

Heme group parameters with several validations can be found in Capece et al., 2013.³⁷ The procedure described above was validated and widely used in several studies of heme proteins from our group^{12,38–41} and in particular for ferrous 5c heme protein complexes.^{38,41–44}

All MD simulations were performed using periodic boundary conditions with a 9 Å cutoff and the particle mesh Ewald (PME) summation method for treating the electrostatic interactions. The covalent bonds involving hydrogen atoms were restrained at their equilibrium distance by using the SHAKE algorithm, while the temperature and pressure were kept constant with a Berendsen thermostat and barostat, respectively, as implemented in the AMBER14 package.³⁶

We have performed molecular dynamics simulation at low (10 °C) and high (50 °C) temperatures. For each simulated condition, the equilibration protocol consisted of (i) slowly heating the whole system from 0 to the final T for 2 ns at constant volume, with harmonic restraints of 80 kcal/(mol·Å²) for all $C\alpha$ atoms, and (ii) slowly heating from 0 to the final T for 2 ns at constant pressure of the entire system. (iii) After these two steps, we have performed ~100 ns of unconstrained molecular dynamics simulation at constant temperature and pressure in order to obtain systems described by the *NPT* ensemble.

In order to enhance conformation sampling, we generated three replicas starting from the initial crystallographic structure described above, using three different equilibration protocols by varying the equilibration parameters (total simulation time, magnitude of harmonic restraints, etc.). This procedure led to three uncorrelated replicas, obtaining a total simulation time of ~300 ns. In addition, taking different uncorrelated structures from the first replicas and restarting the velocities, we extended the MD trajectories for ~100 ns for each state.

Altogether, we obtained approximately 600 ns of MD trajectories for each studied temperature. All structures were found to be stable during the time scale of the simulations. RMSDs for all system studies were stable after 20–30 ns of MD simulations and remained stable during the time scale of the simulation. RMSF, on the other hand, showed the expected fluctuations in flexible protein portions like loops and terminal regions. All histidines roughly retained the positions observed in the crystal structure, confirming that protonation/tautomer assignment can reproduce the experimental structure.

Finally, the ferrous carbon monoxide (CO) structure was constructed using the crystallographic PDB structure by placing a CO molecule in the sixth coordination position, bound to the iron center. Similar procedures as described above were used to obtain a representative set of parameters for the MD simulations for the CO hexacoordinated complex of the protein. Thermalization and equilibration protocols were similar to those described above. After this step, we obtained approximately 600 ns of MD trajectories for each studied temperature.

Implicit Ligand Sampling (ILS). ILS evaluates the free energy cost of adding a small ligand in a particular position of the system, taking into account different orientations of the ligand. Accessible regions for ligand are characterized by low free energy values.

If those regions are connected by sufficient low free energy regions, an internal pathway (IP) can be defined. It is important to note that this technique allows a simultaneous determination of several different IPs of a protein without introducing any bias.

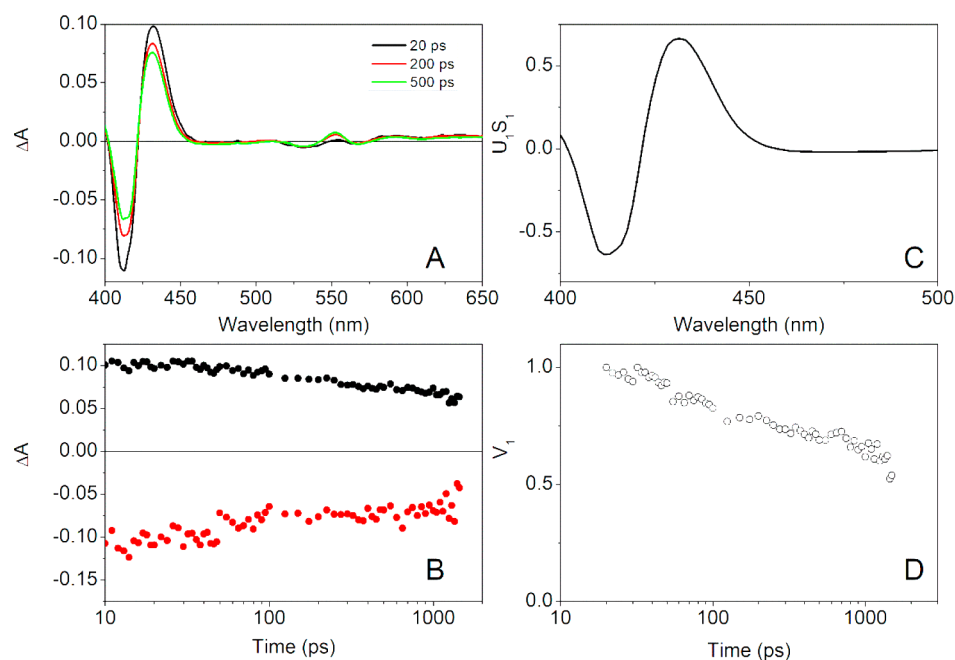


Figure 1. (A) Transient absorption spectra of the CO complex of *Ph*-trHbO excited at 400 nm with femtosecond laser pulses. Spectra are shown at selected delay times: 20 ps (black), 200 ps (red), and 500 ps (green). $T = 20\text{ }^{\circ}\text{C}$, $\text{CO} = 1\text{ atm}$. (B) Kinetic profiles at single wavelengths (red circles, 412 nm; black circles, 432 nm). (C) Singular value decomposition of the TAS data in the Soret range (400–500 nm) for the CO complex of *Ph*-trHbO. The analysis afforded one statistically meaningful spectral component U_1 (singular value $S_1 = 2.56$), which is shown in the top panel, weighted by the corresponding singular value (U_1S_1). (D) Normalized amplitude V_1 is reported as a function of time. Similar results were obtained at the other investigated temperatures.

Technically, the method uses MD simulations of the system without considering the ligand of interest and evaluates the free energy to find the ligand at any positions (and orientations) using a grid. The probability is evaluated in the presence of an “implicit” ligand, considering it as a small perturbation in the Hamiltonian of the original system, described as term of interaction between ligand and protein.^{44,45} ILS has been shown to be a good strategy for prediction of IPs for small neutral ligands in hemoproteins.^{46–50}

In this work, ILS calculations were performed in a regularly spaced rectangular grid of 0.5 \AA resolution that includes the protein. The used probe was a CO molecule, and five different orientations were taken into account. The interaction was considered as a Lennard-Jones term, truncated at 9 \AA . Probe parameters used for the interactions are those corresponding to the AMBER force field, and the geometrical parameters were taken from full-QM geometry optimization for the probe (at the PBE/6-31G** level). The setup used in the ILS calculations and the parameters of the CO probe were validated in several previous works.^{29,47,50–53} Calculations were performed on 4000 frames of each replica described in the previous section. All ILS calculations were performed using the VMD 1.9.1 module program.⁵⁴

To build Figure 4A, we superimposed oxygen atoms on the internal tunnels and cavities identified by the ILS isosurface (we have selected a representative replica). We then removed the ILS surface and left the oxygen atoms instead, depicted as overlapped van der Waals spheres. With this strategy, we get a cleaner graphical representation of the tunnel and cavities. Each point in the free energy profiles of Figure 4B was estimated by finding the minimum cutoff value at which a CO molecule fits within the tunnel and cavities identified with ILS.

Identification of Water Sites. A water site (WS) can be defined as a specific region characterized by high probability of finding a water molecule in comparison to that of finding a water molecule surrounded by the bulk environment. WSs can be identified in an explicit solvent MD simulation.^{3,55,56} A water molecule is considered as occupying a specific WS when the distance between the position of its oxygen atom and the WS center is less than 0.6 \AA . For each identified WS, the following parameters are calculated:

- The water finding probability (WFP), corresponding to the probability of finding a water molecule in the region defined by the WS and normalized with respect to the bulk solvent probability. Only WSs with WFPs values greater than 2 are retained.
- The potential energy associated with the interaction of water molecules inside the WS with the protein and the rest of the solvent is computed.³ For each WS, the total mean interaction energies E_{tot} were computed along 5000 frames of the whole time scale of the MD simulation.

RESULTS

Ligand rebinding kinetics over a temporal range covering 10 orders of magnitude in time was studied using a methodology we have developed for the trHbO of *T. fusca* (*Tf*-trHbO)^{3,29} and that was subsequently applied to the nitric oxide binding protein nitrophorin 7 (NP7) from *Rhodnius prolixus*.^{28,57} The full time course of CO rebinding was determined by merging data obtained from transient absorption spectroscopy with femtosecond excitation (TAS; from 20 ps to 2 ns) and nanosecond laser flash photolysis (LFP; from 20 ns to 100 ms). TAS data collected at times shorter than about 20 ps reflect excited state dynamics and do not provide information

on ligand rebinding.²⁹ Processes occurring on this time scale include formation of transient excited states followed by structural response of the porphyrin macrocycle to the new electronic configuration, and nonradiative relaxation to the electronic ground state.^{58–66} Therefore, this time range has not been considered for further analysis.

Figure 1 (panels A and B) reports transient absorption spectra of *Ph*-trHbO at selected time delays showing the typical features of the difference spectra between carboxy and deoxy species. The decreasing intensity of the signal at increasing delays demonstrates the occurrence of geminate ligand rebinding.

The process was monitored at temperatures from 0 to 40 °C for solutions equilibrated with 1 atm of CO. The rebinding was found to be essentially independent of temperature (see Figure 2). The residual absorbance change at 2 ns further decays at

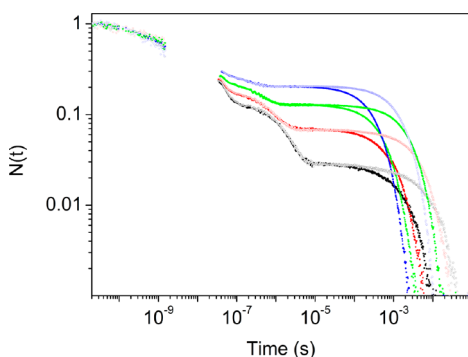


Figure 2. Normalized CO rebinding kinetics to *Ph*-trHbO. The progress curve has been obtained merging the TAS data collected in the subnanosecond range with the data obtained from nanosecond laser flash photolysis. Filled symbols, CO = 1 atm; open symbols, CO = 0.2 atm. $T = 10$ °C (black), 20 °C (red), 30 °C (green), 40 °C (blue).

longer time scales and was followed using nanosecond LFP as a function of temperature (10–40 °C) and CO concentration (solutions were equilibrated with 0.2 and 1 atm CO).

Singular value decomposition analysis of the TAS data in the Soret range (400–450 nm) afforded a single statistically meaningful spectral component (U_1), whose shape resembles the properly scaled steady-state absorption difference spectrum (deoxy-*Ph*-trHbO minus carboxy-*Ph*-trHbO) for the thermally equilibrated ground-state protein (Figure 1C). Time evolution of the amplitude closely follows the absorbance change at 432 nm (Figure 1D).

The amplitudes (V_1) retrieved from SVD at the different temperatures were essentially identical, demonstrating a very weak, if any, temperature dependence of the kinetics in this time range (see the signals at the shortest time scales in Figure 2). The amplitudes V_1 were then merged to the progress curves obtained from nanosecond flash photolysis. Given the lack of distinct spectral components in the SVD analysis, we have followed CO rebinding kinetics after nanosecond photolysis through the absorbance change at 436 nm. Figure 2 reports the full time course of CO rebinding kinetics for *Ph*-trHbO from 20 ps to 100 ms at four different temperatures and two different CO concentrations. The amplitudes retrieved from the SVD analysis on TAS were normalized to 1 assuming unitary photolysis yield. As already explained, the subnanosecond geminate phase of the rebinding kinetics is essentially independent of temperature and CO concentration. Geminate

rebinding extends from the picosecond to microsecond time scale, as evidenced by the lack of sensitivity to CO concentration of this phase.

The time range over which the bimolecular phase occurs is clearly evident in Figure 2, where the curves collected at different CO concentrations diverge at time scales longer than about 10 μ s.

Overall, the rebinding kinetics pattern appears complex, with an unusually long-lived geminate rebinding phase, extending beyond 10 μ s at $T = 10$ °C. As a first approach to the kinetic analysis of the progress curves, we applied a model-independent fitting procedure based on a maximum entropy method (MEM).^{30,31} This allowed the identification of the number of reaction intermediates and the response of their apparent rate constants to temperature and CO concentration.

Figure 3B shows the complex MEM lifetime distributions associated with the rebinding kinetics at two different CO concentrations reported in Figure 3A. Two main time frames can be identified, corresponding to geminate rebinding (from $\sim 10^{-11}$ s to $\sim 10^{-5}$ s) and bimolecular rebinding (on longer time scales). The geminate rebinding kinetics is unaffected by CO concentration as evident from simple visual inspection of Figure 3A. The position of the peaks of the lifetime distribution in the time range from $\sim 10^{-11}$ s to $\sim 10^{-5}$ s (Figure 3B) is essentially unchanged at the two CO pressures, confirming the unimolecular nature of the kinetic phase.

At least three distinct bands are clearly detectable in the geminate rebinding in Figure 3B, corresponding to an equal number of kinetic phases. At 20 °C the bands peak at ~ 1 ns, ~ 30 ns, and ~ 750 ns. A minor amplitude band/shoulder is present at ~ 100 ps. The position of the peak corresponding to the millisecond kinetics in Figure 3B moves to longer times as the CO concentration is decreased because the measured rate constant for the bimolecular phase is proportional to the CO concentration.

The position of the geminate bands at ~ 100 ps, ~ 1 ns, and ~ 30 ns is not significantly affected by temperature (Figure 3C and Figure 3D), demonstrating that for these steps the enthalpic contribution to the activation energy is very small. On the other hand, the position of the longer lived geminate intermediate undergoes a remarkable change with temperature, where the lifetime of ~ 2 μ s at 10 °C becomes 200 ns at 40 °C. Its amplitude is essentially unchanged. The intensity of the band at ~ 30 ns undergoes a drastic drop when the temperature is raised to 40 °C. This decrease in intensity is accompanied by an equivalent increase in the intensity of the band corresponding to bimolecular rebinding, a fact suggesting that the intermediate with 30 ns lifetime is the precursor for the exit to the solvent of the photodissociated ligand. Finally, the kinetic process corresponding to bimolecular rebinding is clearly thermally activated.

MD Simulations at Different Temperatures. In order to address possible differences in the dynamics of *Ph*-trHbO with temperature, we performed MD simulations of the protein at low (10 °C) and high temperature (50 °C).

A close inspection and monitoring of MD simulations indicated that no appreciable differences exist in the global and local structure of the protein at both high and low temperatures, indicating that the protein preserves its overall fold, even at high temperatures. Global fluctuations in the structure of the protein dynamics were addressed using the root mean square deviations (RMSD) analysis, and the local fluctuations were addressed using the root mean square

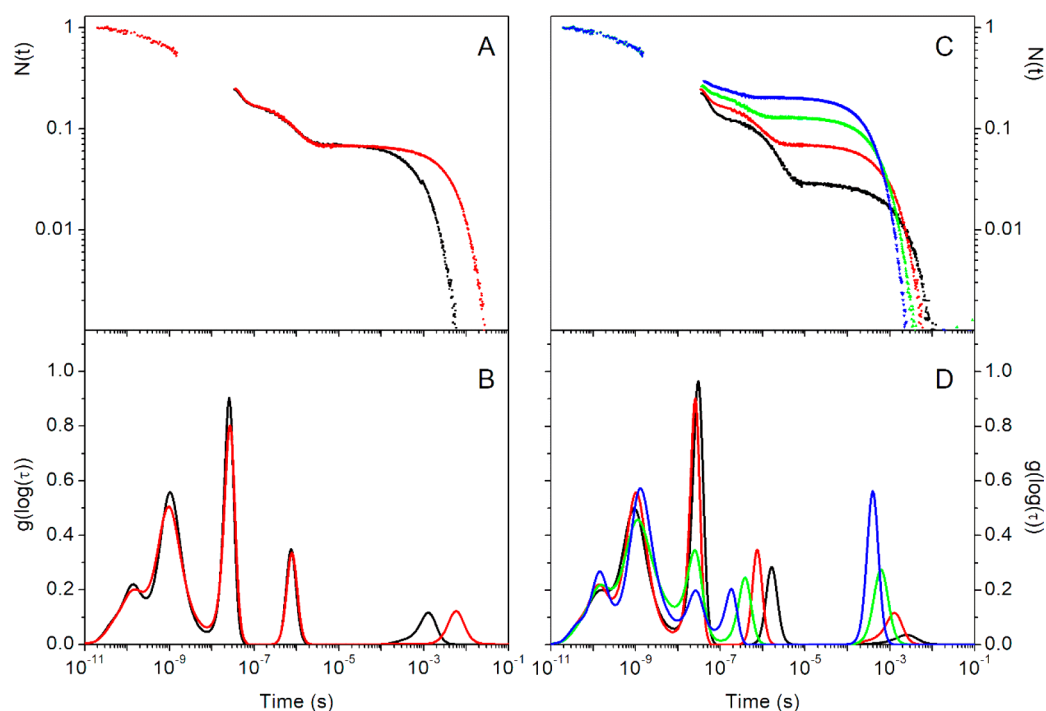


Figure 3. (A) CO rebinding kinetics to *Ph*-trHbO at $T = 20\text{ }^{\circ}\text{C}$ at 1 atm CO (black) and 0.2 atm CO (red). (B) MEM lifetime distributions associated with the rebinding kinetics in panel A. (C) CO rebinding kinetics to *Ph*-trHbO at 1 atm CO as a function of temperature. $T = 10\text{ }^{\circ}\text{C}$ (black), $20\text{ }^{\circ}\text{C}$ (red), $30\text{ }^{\circ}\text{C}$ (green), $40\text{ }^{\circ}\text{C}$ (blue). (D) MEM lifetime distributions associated with the rebinding kinetics in panel C.

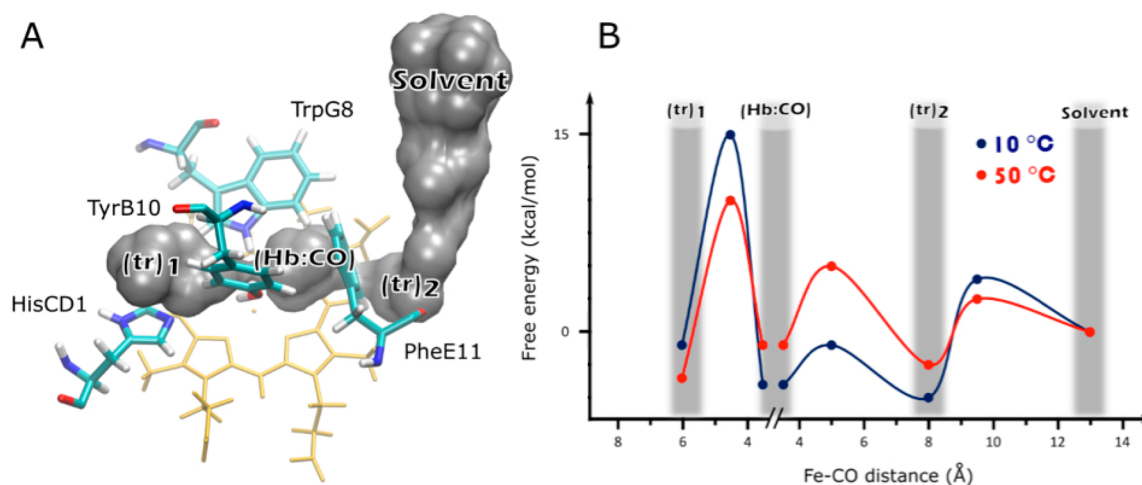


Figure 4. (A) Schematic representation of the heme distal cavity residues of *Ph*-trHbO. The graphical representation of the tunnel and the cavities is explained in the [Methods](#) section. (B) Qualitative estimate of the energetic profile experienced by a ligand along the cavities and the tunnel based on ILS analysis.

fluctuations (RMSF) at both temperatures. The structure of the protein is stable during the time scale of the simulations at both temperatures, and no significant difference between global and local fluctuations was observed by RMSD and RMSF analysis, respectively (data not shown).

Kinetic Analysis. Analysis of the observed rebinding kinetics with a microscopic model requires the identification of a reaction pathway that considers the presence of tunnels and cavities that provide routes for shuttling the ligands to and from the distal cavity within the protein structure.

Implicit ligand sampling (ILS) analysis of the MD simulations on the deoxyferrous protein gave an estimate of the transient cavities formed along the trajectory (Figure 4A). ILS calculations also provide an estimate of the free energy

associated with CO migration inside the potential protein transient tunnel/cavity system at both studied temperatures (Figure 4B). The results show one main tunnel connecting the solvent with an internal cavity system through which small ligands can enter and bind to the Fe atom. This tunnel is similar to the one found in other group-II trHbs, and it has been described as a long tunnel, with mainly hydrophobic features (Figure 4A).³ We detected three docking sites in the protein, located close to the iron atom (Hb:CO) and further away (tr_1 and tr_2) (Figure 4A). The topology of these cavities is in agreement with previous simulations on deoxy Fe(II) and Fe(III) *Ph*-trHbO.¹³

The shape of the cavities described above is similar to that observed for *Tf*-trHbO at room temperature.³ The main

difference with *Tf*-trHbO is in the connectivity of the off-pathway docking site which, for the case of *Ph*-trHbO, is much less connected to the rest of the cavity system.³ At high temperature, we observe a reshaping of the cavity/tunnel distribution where the energetic barrier separating $(tr)_1$ from the distal pocket undergoes a remarkable increase.

Figure 4A also depicts four distinctive amino acids surrounding the vicinity of the iron heme group. The connection between the solvent and the first docking site $((tr)_2)$ does not present any bulky amino acid blocking the access of the CO. However, the connection between $(tr)_2$ and (Hb:CO) is partly hindered by PheE11. In addition, the connection between (Hb:CO) and $(tr)_1$ is inhibited by the presence TrpG8 and TyrB10. Finally, we did not observe fluctuations in the position of the amino acids surrounding the cavity system.

The CD1 position is occupied by His in *Ph*-trHbO, whereas *Tf*-trHbO has Tyr. For the case of *Ph*-trHbO, we observed one preferential conformation for HisCD1, having no impact on the access of CO to the off-pathway cavity $(tr)_1$.

On the basis of the above evidence, we have sketched a kinetic model that takes into account the topology of the connections between inner cavities and is reported in Scheme 1. Data collected at 1 and 0.2 atm of CO were globally fitted using this scheme, where concentrations were held fixed and rate constants were optimized.

It should be mentioned that a distal Tyr was reported to complete coordination of the Fe(II) in the unliganded *Ph*-trHbO.^{12,67} However, as previously reported, we did not find any sign of competition in the ligand binding kinetics,¹³ and this kinetic step was accordingly not considered.

The optimization was started from a set of parameters where the on-pathway cavity $(tr)_2$ is populated with higher rate (rates k_+ and k_-) than the off-pathway cavity $(tr)_1$ (rates k_d and k_{-d}). Optimization leads to values for the rate constants such that $(tr)_2$ modulates the geminate rebinding kinetics in the picoseconds–short nanoseconds time scale and $(tr)_1$ is responsible for the geminate rebinding kinetics in the microseconds. An alternative starting set of parameters was tried, where the cavity $(tr)_2$ is populated with lower rate than $(tr)_1$. Although this provided an equivalent good fit, the results were discarded because the energetic barriers did not comply with those retrieved from ILS analysis (Figure 4).

The overall rebinding curve is reproduced correctly by the above model, as can be appreciated in the representative global fit performed on the traces at 1 and 0.2 atm of CO for $T = 20$ °C reported in Figure 5A. We point out that the missing range between 2 and 20 ns may admittedly contain minor kinetic features that would go undetected in our experiment and are ignored in our kinetic model. Hence, filling this gap appears as a needed improvement for future developments.

From the Eyring plot of the microscopic rate constants determined at each temperature (Figure 5B), it is possible to estimate the activation entropy and enthalpy for each rate constant. These parameters are reported in Table 1 along with the activation free energy at 20 °C.

DISCUSSION

The use of a microscopic model⁶⁸ to describe the progress curve from picosecond geminate to millisecond bimolecular rebinding allows us to decompose the overall kinetics into its constitutive elementary steps and gain deeper insight into the coupling between molecular dynamics and function.²⁵

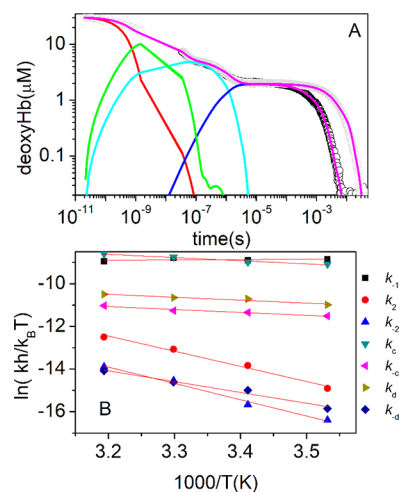


Figure 5. (A) Representative global fit of CO rebinding kinetics to *Ph*-trHbO for solutions equilibrated with 1 and 0.2 atm CO. $T = 20$ °C. The legend in the figure identifies reaction intermediates. The color code matches the one used in Scheme 1: red, (Hb:CO); cyan, $(tr)_1$; green, $(tr)_2$; blue, Hb; magenta, fit. Open circles are the data collected at the two CO partial pressures. (B) Eyring plot of the microscopic rate constants determined from the global fit of the rebinding curves at the two CO concentrations used at each temperature.

Given the similar fold and the presence of an alike system of cavities within the protein matrix, it is natural to compare the ligand binding kinetics to *Ph*-trHbO with that of the related thermophilic *Tf*-trHbO^{3,29} in order to identify possible signatures of cold adaptation. The rate k_{-1} for *Ph*-trHbO is larger than for *Tf*-trHbO, for which we estimated 3.0×10^8 s⁻¹ at 20 °C.²⁹ As found for *Tf*-trHbO, the free energy barrier is mostly entropic in nature but slightly lower (5 kcal/mol for *Ph*-trHbO vs 5.8 kcal/mol for *Tf*-trHbO). The value of k_{-1} and the corresponding kinetic barrier are similar to those observed for the *Tf*-trHbO triple mutant YB10F-YCD1F-WG8F (3F).³ A larger value for k_{-1} was estimated for the *Tf*-trHbO WG8F mutant in response to a lower entropic contribution to the barrier, possibly related to a smaller volume of the distal cavity in comparison to that of the *Tf*-trHbO 3F mutant.

The rebinding rates k_{-1} for *Ph*-trHbO and *Tf*-trHbO are remarkably high if compared to other Hbs, for which typical values are on the order of 10^6 – 10^7 s⁻¹.^{25,69–71} However, much higher rates were reported for nitrophorins 4⁷² and 7^{28,57} from *R. prolixus* for which pH dependent values are in the order of 10^9 – 10^{10} s⁻¹. The reason for these exceptionally high rates may be partly found in the distorted heme in these proteins.^{28,72}

Internal migration rates (k_c , k_{-c} , k_d , and k_{-d}) at 20 °C are comparable to those for the *Tf*-trHbO mutants, but the barriers have in general appreciable enthalpic contributions, which makes these kinetic steps sensitive to temperature. In particular, in order to exit from the kinetic trap $(tr)_1$, a remarkable energy barrier has to be overcome (10 kcal/mol for rate k_{-d}). This is evident in the temperature dependence of the lifetime distribution in Figure 3D, where the relevant band for depopulation of the kinetics trap $(tr)_1$ shifts from 200 ns at 40 °C to 2 μs at 10 °C.

The presence of such an efficient and stable trap for the photodissociated ligands may have functional significance for multistep reactions like those involved in removal of

Table 1. Optimized Microscopic Rate Constants at $T = 20\text{ }^{\circ}\text{C}$ for CO Rebinding to *Ph*-trHbO as Derived from Reaction Scheme 1^a

rate	ΔS^{\ddagger} (cal/(mol K))	ΔH^{\ddagger} (kcal/mol)	ΔG^{\ddagger} (kcal/mol)		
			<i>Ph</i> -trHbO	<i>Tf</i> -trHbO	
k_{-1} (s^{-1})	8.37×10^8	-18 ± 2	-0.3 ± 0.6	5 ± 1	5.8 ± 0.1
k_2 (s^{-1})	6.0×10^6	20 ± 4	14 ± 1	8 ± 2	7 ± 3 (6 ± 4 , 20%)
k_{-2} ($\text{M}^{-1} \text{s}^{-1}$)	9.53×10^5	21 ± 4	15 ± 1	9 ± 2	8 ± 3 (6 ± 10 , 20%)
k_c (s^{-1})	7.67×10^8	-8 ± 1	3.0 ± 0.3	5.2 ± 0.6	6.0 ± 0.1
k_{-c} (s^{-1})	0.72×10^8	-13 ± 1	2.7 ± 0.4	6.6 ± 0.7	8.7 ± 0.1
k_d (s^{-1})	1.36×10^8	-12 ± 2	2.7 ± 0.4	6 ± 1	7.1 ± 0.1
k_{-d} (s^{-1})	1.88×10^6	4 ± 3	10 ± 1	9 ± 2	7.9 ± 0.4

^aActivation enthalpies ΔH^{\ddagger} and entropies ΔS^{\ddagger} were estimated from the linear Eyring plots for each rate constant k_i in the temperature range of 10–40 $^{\circ}\text{C}$, according to the equation $\ln(hk_i/(k_B T)) = \Delta S^{\ddagger}/R - \Delta H^{\ddagger}/(RT)$, where R is the gas constant, h is Planck's constant, and k_B is Boltzmann constant. The free energy at 20 $^{\circ}\text{C}$ is calculated from the definition $\Delta G^{\ddagger} = \Delta H^{\ddagger} - T\Delta S^{\ddagger}$. For comparison, ΔG^{\ddagger} data for *Tf*-trHbO are also reported.³

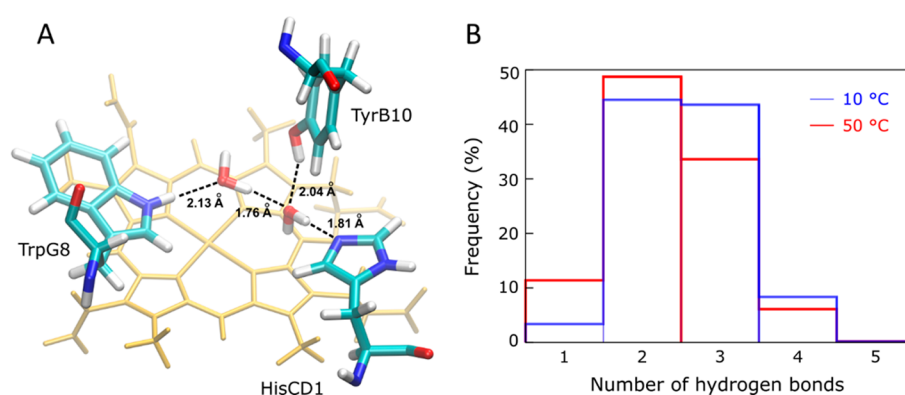


Figure 6. (A) Position of the two water molecules identified in *Ph*-trHbO by the MD simulations. They are mainly stabilized by hydrogen bond interactions with residues TyrB10, HisCD1, and TrpG8. (B) Average percentage of hydrogen bonds between residues and water (water–water hydrogen bond is not considered in the percentages), along the MD simulations run at 10 and 50 $^{\circ}\text{C}$.

reactive oxygen and nitrogen species. *Ph*-trHbO is indeed involved in the protection against reactive nitrogen species.¹⁴ The role of hydrophobic cavities in sustaining the turnover in NO dioxygenase reactions was suggested by Brunori for neuroglobin⁷³ and myoglobin.⁷⁴ Trapping of photodissociated ligands within internal cavities was demonstrated for several Hbs with various experimental methods including low temperature⁷⁵ and time-resolved⁷⁶ X-ray crystallography, temperature derivative FTIR spectroscopy,⁷⁷ and laser flash photolysis.^{34,78} However, the case of *Ph*-trHbO appears as one of the longest lived and most highly populated reaction intermediates observed at room temperature and low viscosity reported to date.

The rate constants for exit to (k_2) and return from the solvent (k_{-2}) are smaller than those determined for *Tf*-trHbO. This is due to quite large free energy barriers for the two rates (Table 1). For these processes, sizable enthalpic contributions result in temperature-dependent rate constants as evident from the shift of the bimolecular rebinding band in Figure 3D, centered at $\sim 400\ \mu\text{s}$ at 40 $^{\circ}\text{C}$ and $\sim 3\ \text{ms}$ at 10 $^{\circ}\text{C}$.

Unlike *Tf*-trHbO,²⁹ bimolecular rebinding is a homogeneous process and does not appear to reflect the presence of multiple functional conformations in the protein.

It is useful to estimate the bimolecular binding rate constant, usually termed k_{on} , which for *Ph*-trHbO is $0.95 \times 10^6\ \text{M}^{-1}\ \text{s}^{-1}$ at 20 $^{\circ}\text{C}$. This value is similar to the one determined for the open conformation of *Tf*-trHbO, for which $k_{\text{on}} = 0.93 \times 10^6\ \text{M}^{-1}\ \text{s}^{-1}$ at 20 $^{\circ}\text{C}$. The closed conformation in *Tf*-trHbO,

accounting for 80% of the rebinding, is characterized by $k_{\text{on}} = 8.7 \times 10^4\ \text{M}^{-1}\ \text{s}^{-1}$ at the same temperature. These figures increase to $2.75 \times 10^6\ \text{M}^{-1}\ \text{s}^{-1}$ and $1.63 \times 10^5\ \text{M}^{-1}\ \text{s}^{-1}$ at 25 $^{\circ}\text{C}$.

Structural and Dynamical Determinants of the Observed Kinetics. The heme distal site in the crystal structure of deoxy *Ph*-trHbO hosts a structured H-bond network that involves TyrB10, HisCD1, TrpG8, and two water molecules.¹³ The heme pocket coordinated water molecule is H-bonded to a second water molecule and to the indole NE1 atom of TrpG8. The latter water molecule is fully buried in the distal site and H-bonded to the TyrB10 hydroxyl group and to the NE2 atom of HisCD1.

A similar picture emerges also from MD simulations, showing that water molecules can access the heme distal pocket and are stabilized through an H-bond network based on the distal residues TyrB10, HisCD1, and TrpG8 (Figure 6A).¹³ The stabilization of these molecules does not involve Fe(II) as no solvent molecules are coordinated to the metal center.

In order to detect possible changes in the H-bond network with temperature, MD simulations were run at 10 and 50 $^{\circ}\text{C}$.

During the time scale of the MD simulations, two or three hydrogen bonds between water molecules and the amino acid residues were detected with the highest probability (Figure 6B). In addition, a hydrogen bond between the two water molecules was observed. The number of hydrogen bonds slightly decreases when temperature is increased (Figure 6B) due to a more rapid exchange of water promoted by an

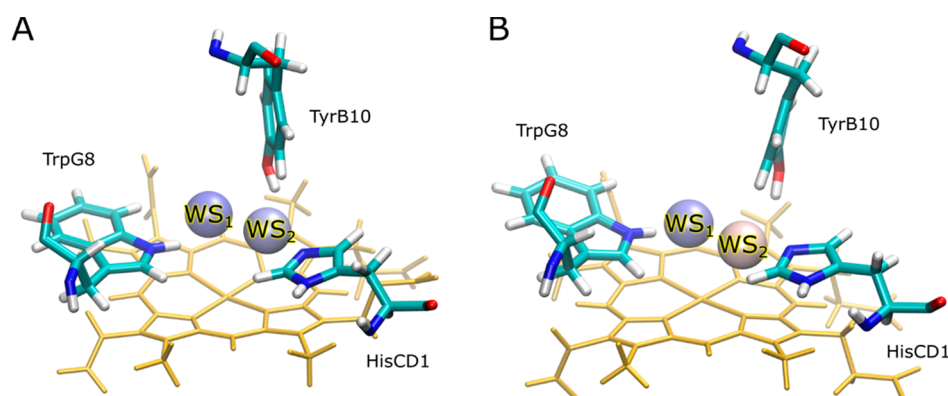


Figure 7. Schematic representation of WSs surrounding the heme group at $T = 10\text{ }^{\circ}\text{C}$ (A) and $T = 50\text{ }^{\circ}\text{C}$ (B). WSs are depicted as balls from high to low probability on a blue to red color scale.

increase in the conformational population for which a direct hydrogen bond interaction between HisCD1 and TyrB10 occurs and leads to release of the coordinated water molecule.

Analysis of the dynamics of the water molecules in the distal cavity by WS calculations reveals that the two water molecules are not equivalent. In particular, the probability (WFP) of finding each water molecule in the particular position inside the ligand-recognition cavity with respect to the solvent, and the average interaction energy are different, as shown in Figure 7 and Table 2.

Table 2. WS Characteristic Parameters (WFP (Water Finding Probability) and Average Interaction Energy E_{tot}) of Each WS Obtained from the MD Simulations at Low and High Temperatures^a

	<i>Ph-trHbO</i>				<i>Tf-trHbO</i> , ³ WS ₁ 27 °C
	WS ₁		WS ₂		
	10 °C	50 °C	10 °C	50 °C	
WFP	11.1	3.4	9.9	2.5	19.2
E_{tot} (kcal/mol)	-1.6	-1.1	-8.2	-6.8	-14.8

^aFor comparison, the same parameters estimated for *Tf-trHbO* at room temperature are reported.

Table 2 shows that the WFP values for WS₁ are higher compared to those obtained for WS₂ at both temperatures, while the interaction energy has an opposite trend. In addition, WFP values decrease when temperature is increased for both WS, possibly due to a faster water exchange with the solvent. As explained above, a significant population in which a direct hydrogen bond interaction between HisCD1 and TyrB10 is present seems to promote water exchange with the solvent in the vicinity of the WS₂. On the other hand, WS₁ presents less favorable interaction energy than WS₂, although they both have similar WFP values. It is worth pointing out that there is a 3- to 4-fold decrease in WFP between low and high temperature for both WS, whereas E_{tot} is approximately the same. This suggests that WS stabilization is basically entropically driven. More quantitative estimates are made difficult by the limited available conformational sampling.

In order to assess the influence of ligation on the solvent molecules in the distal cavity, MD simulations were run on the carboxy *Ph-trHbO* structure. For this case, water molecules in the active site were not observed, and a hydrogen bond between the CO and the TrpG8 residue was present during the

whole time scale of the simulation (at both low and high temperature), in keeping with previous results.¹³

Comparison with the carboxy *Ph-trHbO* structure (Figure 8) demonstrates that the environment in the distal pocket for

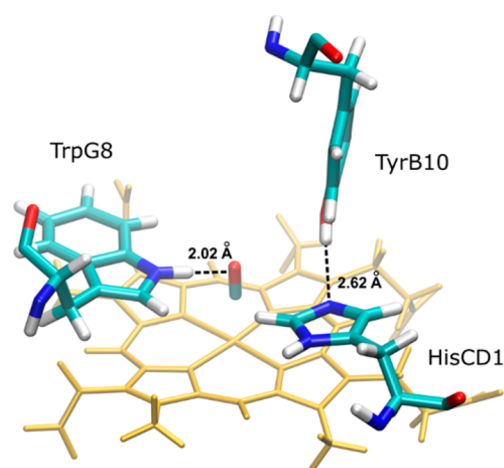


Figure 8. Close-up of the distal pocket residues of carboxy *Ph-trHbO* where the hydrogen bond between CO and TrpG8 is shown.

deoxy *Ph-trHbO* requires only a minimal structural rearrangement to accommodate the water molecules after CO photodissociation. These rearrangements occur on picosecond to nanosecond time scales and are expected to allow water entry to identified WSs from nearby positions, identified in MD simulations on the CO-bound heme state.

As we have already observed, the value of the rate constant k_{-1} for CO binding to the heme from the distal pocket (Hb:CO) reported in Table 1 is similar to the one we have determined for the triple mutant YB10F-YCD1F-WG8F of *Tf-trHbO*.³ In that case, the value of the rate constant k_{-1} was intermediate between that of the wt protein ($3.0 \times 10^8\text{ s}^{-1}$) and that of the WG8F mutant, for which a value of $20 \times 10^8\text{ s}^{-1}$ was determined. In the case of *Tf-trHbO*, the enhancement was discussed in terms of destabilization of water molecules in the distal cavity.

The use of water molecules for tuning reactivity in the distal cavity appears as a general strategy capable of exploiting the peculiar properties of water for achieving temperature adaptation.

It was reported that the main barrier to ligand binding to deoxy-trHbN from mesophilic *Mycobacterium tuberculosis* (*Mt-*

trHbN) is the displacement of a distal cavity water molecule, stabilized by interactions with TyrB10 and GlnE11 but not coordinated to the heme iron.¹⁹ Mutations of TyrB10/GlnE11 to apolar amino acids resulted in much faster ligand (CO and O₂) binding, with k_{on} approaching $10^9 \text{ M}^{-1} \text{ s}^{-1}$. NO rebinding experiments to Fe(III) *Mt*-trHbN allowed us to demonstrate fast (ns) water rebinding, held responsible for a low geminate recombination.

On the other hand, ultrafast ligand recombination in trHbO from *Mycobacterium tuberculosis* (*Mt*-trHbO) demonstrated that 95% of the photodissociated CO molecules are rebound within 1.2 ns. This finding was rationalized on the basis of the results of MD simulations that showed a layer of water molecules surrounding the distal pocket and imposing a relevant barrier to ligand escape by restricting the effective distal pocket volume.⁴ Although it is not possible to compare the stability of WS for *Mt*-trHbO with our estimates for *Ph*-trHbO (Table 2), we can presume that water molecules are much more stable in *Mt*-trHbO than in *Ph*-trHbO.

Water molecules are present in the distal cavity of Fe(II) *Ph*-trHbO, both in the crystal structure and in the MD simulations. These molecules occupy the space region that is normally taken by the ligand (e.g., CO) when it is bound to Fe(II). Indeed, water molecules are not present in the MD simulations on CO-*Ph*-trHbO. Therefore, when CO enters, rearrangement of water molecules is needed, which imposes a kinetic barrier on rebinding (rate k_{-1}). The weaker interaction energy E_{tot} and the lower WFP make the rate comparable to the one for the 3F mutant of *Tf*-trHbO.

In comparison to *Ph*-trHbO, the overall interaction energy for WS₁ in *Tf*-trHbO is in fact much more favorable for the wt (−14.8 kcal/mol), comparable for WG8F (−8.5 kcal/mol), and less favorable for 3F *Tf*-trHbO (−2.6 kcal/mol).³

Similarly, when it comes to WFP, the probability of finding a water molecule near the iron atom of the heme group in the distal pocket of *Ph*-trHbO at $T = 10 \text{ }^\circ\text{C}$ (Table 2) is comparable to the one calculated for the WG8F mutant of *Tf*-trHbO at $T = 20 \text{ }^\circ\text{C}$. The values for WFP values of *Tf*-trHbO are 19.2, 11.6, and 2.5 for wt, WG8F, and 3F *Tf*-trHbO, respectively.³ In conclusion, coordination of water molecules is much tighter in *Tf*-trHbO than in *Ph*-trHbO.

Although it seems reasonable to expect an active role for the water molecules also in the opposite temperature response of energetic barriers separating (Hb:CO) from (tr)₁ and (tr)₂, reported in Figure 4B, this contribution has not been clearly identified yet. This issue will require further investigations in order to assess also the role of the change in the mobility of side chains of relevant amino acids.

Spectrokinetic studies on myoglobin reported the possibility of detecting the presence of water molecules in the distal pocket through their effects on the spectral shape in the Q absorption bands, where entry of water molecules leads to small but detectable spectral shift.^{79,80} The low intensity of Q bands and the overlapping excited state absorption at short times severely limit the sensitivity in this spectral range. SVD analysis of the TAS data in the Q-band region afforded a main spectral component, with the characteristic shape of the deoxy *Ph*-trHbO minus carboxy *Ph*-trHbO spectrum (Figure 9). A minor spectral component, which could be attributed to solvation effects in the distal pocket, was evident only at $T = 0 \text{ }^\circ\text{C}$ and not at higher temperatures, an indication that water is stabilized in the distal pocket only at low temperature. The spectral shape is consistent with literature data.^{79,80} The time

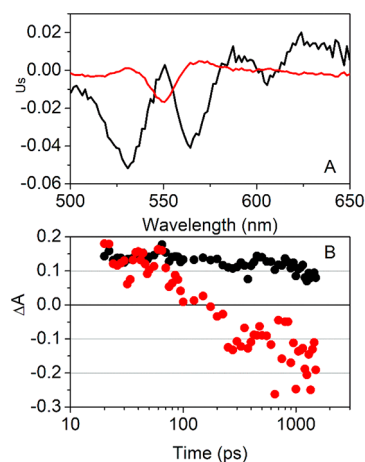


Figure 9. Singular value decomposition of the TAS data in the Q bands at $T = 0 \text{ }^\circ\text{C}$. (A) The analysis afforded a major spectral component U_1 (black curve, singular value $S_1 = 0.37$) and a minor spectral component U_2 (red curve, singular value $S_2 = 0.06$). (B) Corresponding amplitudes (black, V_1 ; red, V_2) as a function of time. $T = 0 \text{ }^\circ\text{C}$, CO = 1 atm.

course of the amplitude V_1 is in keeping with ligand binding reported in Figure 1 (normalized curves overlap). The second component shows a change in sign as previously reported for myoglobin and some of its mutants.^{79,80} Given the limited time range covered by the subnanosecond experiment, it is not possible to follow the entire time course so that only entry of water molecules after photodissociation is detected. The time course of V_2 is best described by an exponential relaxation with a lifetime of 190 ps, which may be interpreted as the time scale for water being coordinated by amino acids in the distal pocket.

The above experimental and computational evidence strongly indicates that mechanisms leading to water stabilization in the distal pocket of *Ph*-trHbO are weakened. Destabilization of water molecules in the distal pocket, where the ligand binds to the Fe atom, may be taken as an indication of cold adaptation in the reaction mechanism. Cold adaptation in enzymes was suggested to exploit water dislocation to simultaneously increase entropy and decrease enthalpy.⁸¹ If more water molecules are released upon entry of the ligand to the reaction site, where the transition state is expected to form, than in the absence of the ligand, then there will be considerable entropic benefit for the formation of a transition state complex.^{81,82} The lower stabilization of water molecules in the distal pocket of *Ph*-trHbO then leads to an activation entropy for ligand binding to the Fe atom which is comparable to the one observed for the mutant 3F *Tf*-trHbO, where the water stabilizing interactions are removed from the distal pocket by changing the chemical nature of the amino acids lining the cavity.

CONCLUSIONS

The CO rebinding kinetics to the cold adapted *Ph*-trHbO is characterized by a multiphasic progress curve with peculiar features. As reported for other truncated Hbs, geminate rebinding is found to begin in the picosecond time scale. An unusually large and long-lived geminate recombination extends to the microseconds and is rationalized in terms of migration to an off-pathway internal cavity, separated by the distal pocket by a rather large energy barrier, with a remarkable enthalpic

contribution. Migration of the ligand to/from the solvent is modeled to occur through an articulated system of tunnels and cavities that tunes rebinding.

Water molecules in the distal pocket tune the rebinding rate, but the weak stabilization of the solvent molecules appears to favor binding of the ligand through entropic effects. Comparison with the related thermophilic Tf-trHbO suggests that this mechanism may reflect cold adaptation of the protein.

AUTHOR INFORMATION

Corresponding Author

*E-mail: cristiano.viappiani@unipr.it

ORCID

Dario Estrin: 0000-0002-5006-7225

Barbara Patrizi: 0000-0003-2696-1611

Mariangela Di Donato: 0000-0002-6596-7031

Cristiano Viappiani: 0000-0001-7470-4770

Notes

The authors declare no competing financial interest.

ACKNOWLEDGMENTS

This study was carried out in the framework of the SCAR program “Antarctic Thresholds: Ecosystem Resilience and Adaptation” (AnT-ERA). C.V., D.G., and S.B. acknowledge financial support by the Italian National Programme (PdR 2013/AZ1.20) for Antarctic Research (PNRA). D.E. and L.B. acknowledge funding from Universidad de Buenos Aires (Grant UBACYT 20020130100097BA) and Agencia Nacional de Promocion Cientifica y Tecnologica Grants PICT 2014-1022, PICT 2015-2761, and 2015-2989. L.B. acknowledges Bunge & Born Foundation for financial support. S.A. and C.V. acknowledge Azienda USL di Piacenza and Fondazione di Piacenza e Vigevano for financial support. C.V. acknowledges S. E. Braslavsky for the kind donation of the Spectron laser. All computer simulations were run at Centro de Computo de Alto Rendimiento (CECAR). This project has received funding from the European Union’s Horizon 2020 Research and Innovation Programme under Grant 654148 Laserlab-Europe (Laserlab-Europe, H2020 EC-GA 654148).

REFERENCES

- (1) Siddiqui, K. S.; Cavicchioli, R. Cold-adapted enzymes. *Annu. Rev. Biochem.* **2006**, *75*, 403–433.
- (2) Siddiqui, K. S.; Williams, T. J.; Wilkins, D.; Yau, S.; Allen, M. A.; Brown, M. V.; Lauro, F. M.; Cavicchioli, R. Psychrophiles. *Annu. Rev. Earth Planet. Sci.* **2013**, *41*, 87–115.
- (3) Bustamante, J. P.; Abbruzzetti, S.; Marcelli, A.; Gauto, D.; Boechi, L.; Bonamore, A.; Boffi, A.; Bruno, S.; Feis, A.; Foggi, P.; et al. Ligand uptake modulation by internal water molecules and hydrophobic cavities in hemoglobins. *J. Phys. Chem. B* **2014**, *118*, 1234–1245.
- (4) Jasaitis, A.; Ouellet, H.; Lambry, J. C.; Martin, J. L.; Friedman, J. M.; Guertin, M.; Vos, M. H. Ultrafast heme-ligand recombination in truncated hemoglobin HbO from *Mycobacterium tuberculosis*: a ligand cage. *Chem. Phys.* **2012**, *396*, 10–16.
- (5) Paredes, D. I.; Watters, K.; Pitman, D. J.; Bystroff, C.; Dordick, J. S. Comparative void-volume analysis of psychrophilic and mesophilic enzymes: Structural bioinformatics of psychrophilic enzymes reveals sources of core flexibility. *BMC Struct. Biol.* **2011**, *11*, 42.
- (6) Vinogradov, S. N.; Hoogewijs, D.; Bailly, X.; Arredondo-Peter, R.; Gough, J.; Dewilde, S.; Moens, L.; Vanfleteren, J. R. A phylogenomic profile of globins. *BMC Evol. Biol.* **2006**, *6*, 31.

(7) Vinogradov, S. N.; Hoogewijs, D.; Bailly, X.; Mizuguchi, K.; Dewilde, S.; Moens, L.; Vanfleteren, J. R. A model of globin evolution. *Gene* **2007**, *398*, 132–142.

(8) Vinogradov, S. N.; Moens, L. Diversity of globin function: enzymatic, transport, storage, and sensing. *J. Biol. Chem.* **2008**, *283*, 8773–8777.

(9) Pathania, R.; Navani, N. K.; Gardner, A. M.; Gardner, P. R.; Dikshit, K. L. Nitric oxide scavenging and detoxification by the *Mycobacterium tuberculosis* haemoglobin, HbN in *Escherichia coli*. *Mol. Microbiol.* **2002**, *45*, 1303–1314.

(10) Wittenberg, J. B.; Bolognesi, M.; Wittenberg, B. A.; Guertin, M. Truncated hemoglobins: a new family of hemoglobins widely distributed in bacteria, unicellular eukaryotes, and plants. *J. Biol. Chem.* **2002**, *277*, 871–874.

(11) Ascenzi, P.; Bolognesi, M.; Milani, M.; Guertin, M.; Visca, P. Mycobacterial truncated hemoglobins: From genes to functions. *Gene* **2007**, *398*, 42–51.

(12) Howes, B. D.; Giordano, D.; Boechi, L.; Russo, R.; Mucciacciaro, S.; Ciaccio, C.; Sinibaldi, F.; Fittipaldi, M.; Martí, M. A.; Estrin, D. A.; et al. The peculiar heme pocket of the 2/2 hemoglobin of cold-adapted *Pseudoalteromonas haloplanktis* TAC125. *JBIC, J. Biol. Inorg. Chem.* **2011**, *16*, 299–311.

(13) Giordano, D.; Pesce, A.; Boechi, L.; Bustamante, J. P.; Caldelli, E.; Howes, B. D.; Riccio, A.; di Prisco, G.; Nardini, M.; Estrin, D.; et al. Structural flexibility of the heme cavity in the cold-adapted truncated hemoglobin from the Antarctic marine bacterium *Pseudoalteromonas haloplanktis* TAC125. *FEBS J.* **2015**, *282*, 2948–2965.

(14) Coppola, D.; Giordano, D.; Tinajero-Trejo, M.; di Prisco, G.; Ascenzi, P.; Poole, R. K.; Verde, C. Antarctic bacterial haemoglobin and its role in the protection against nitrogen reactive species. *Biochim. Biophys. Acta, Proteins Proteomics* **2013**, *1834*, 1923–1931.

(15) Giordano, D.; Coppola, D.; Russo, R.; Tinajero-Trejo, M.; di Prisco, G.; Lauro, F.; Ascenzi, P.; Verde, C. In *Advances in Microbial Physiology*; Poole, R. K., Ed.; Academic Press, 2013; Vol. 63, pp 329–389.

(16) Coppola, D.; Giordano, D.; Milazzo, L.; Howes, B. D.; Ascenzi, P.; di Prisco, G.; Smulevich, G.; Poole, R. K.; Verde, C. Coexistence of multiple globin genes conferring protection against nitrosative stress to the Antarctic bacterium *Pseudoalteromonas haloplanktis* TAC125. *Nitric Oxide* **2018**, *73*, 39–51.

(17) Pesce, A.; Couture, M.; Dewilde, S.; Guertin, M.; Yamauchi, K.; Ascenzi, P.; Moens, L.; Bolognesi, M. A novel two-over-two α -helical sandwich fold is characteristic of the truncated hemoglobin family. *EMBO J.* **2000**, *19*, 2424–2434.

(18) Milani, M.; Pesce, A.; Ouellet, Y.; Dewilde, S.; Friedman, J.; Ascenzi, P.; Guertin, M.; Bolognesi, M. Heme-ligand tunneling in group I truncated hemoglobins. *J. Biol. Chem.* **2004**, *279*, 21520–21525.

(19) Ouellet, Y. H.; Daigle, R.; Lagüe, P.; Dantsker, D.; Milani, M.; Bolognesi, M.; Friedman, J. M.; Guertin, M. Ligand binding to truncated hemoglobin N from *Mycobacterium tuberculosis* is strongly modulated by the interplay between the distal heme pocket residues and internal water. *J. Biol. Chem.* **2008**, *283*, 27270–27278.

(20) Russo, R.; Giordano, D.; di Prisco, G.; Hui Bon Hoa, G.; Marden, M. C.; Verde, C.; Kiger, L. Ligand-rebinding kinetics of 2/2 hemoglobin from the Antarctic bacterium *Pseudoalteromonas haloplanktis* TAC125. *Biochim. Biophys. Acta, Proteins Proteomics* **2013**, *1834*, 1932–1938.

(21) Giordano, D.; Parrilli, E.; Dettai, A.; Russo, R.; Barbiero, G.; Marino, G.; Lecointre, G.; di Prisco, G.; Tutino, L.; Verde, C. The truncated hemoglobins in the Antarctic psychrophilic bacterium *Pseudoalteromonas haloplanktis* TAC125. *Gene* **2007**, *398*, 69–77.

(22) Delcanale, P.; Pennacchietti, F.; Maestrini, G.; Rodríguez-Amigo, B.; Bianchini, P.; Diaspro, A.; Iagatti, A.; Patrizi, B.; Foggi, P.; Agut, M.; et al. Subdiffraction localization of a nanostructured photosensitizer in bacterial cells. *Sci. Rep.* **2015**, *5*, 15564.

(23) Park, H.; Heldman, N.; Rebentrost, P.; Abbondanza, L.; Iagatti, A.; Alessi, A.; Patrizi, B.; Salvalaggio, M.; Bussotti, L.; Mohseni, M.;

et al. Enhanced energy transport in genetically engineered excitonic networks. *Nat. Mater.* **2016**, *15*, 211.

(24) Iagatti, A.; Patrizi, B.; Basagni, A.; Marcelli, A.; Alessi, A.; Zanardi, S.; Fusco, R.; Salvalaggio, M.; Bussotti, L.; Foggi, P. Photophysical properties and excited state dynamics of 4,7-dithien-2-yl-2,1,3-benzothiadiazole. *Phys. Chem. Chem. Phys.* **2017**, *19*, 13604–13613.

(25) Abbruzzetti, S.; Bruno, S.; Faggiano, S.; Grandi, E.; Mozzarelli, A.; Viappiani, C. Time-resolved methods in Biophysics. 2. Monitoring haem proteins at work with nanosecond laser flash photolysis. *Photochem. Photobiol. Sci.* **2006**, *5*, 1109–1120.

(26) Henry, E. R.; Hofrichter, J. In *Numerical Computer Methods*; Brand, L., Johnson, M. L., Eds.; Academic Press, Inc.: San Diego, CA, 1992; Vol. 210, pp 129–192.

(27) Abbruzzetti, S.; He, C.; Ogata, H.; Bruno, S.; Viappiani, C.; Knipp, M. Heterogeneous kinetics of the carbon monoxide association and dissociation reaction to Nitrophorin 4 and 7 coincide with structural heterogeneity of the gate-loop. *J. Am. Chem. Soc.* **2012**, *134*, 9986–9998.

(28) Knipp, M.; Ogata, H.; Soavi, G.; Cerullo, G.; Allegri, A.; Abbruzzetti, S.; Bruno, S.; Viappiani, C.; Bidon-Chanal, A.; Luque, F. J. Structure and dynamics of the membrane attaching nitric oxide transporter nitrophorin 7. *F1000Research* **2015**, *4*, 45.

(29) Marcelli, A.; Abbruzzetti, S.; Bustamante, J. P.; Feis, A.; Bonamore, A.; Boffi, A.; Gellini, C.; Salvi, P. R.; Estrin, D. A.; Bruno, S.; et al. Following ligand migration pathways from picoseconds to milliseconds in type II truncated hemoglobin from *Thermobifida fusca*. *PLoS One* **2012**, *7*, e39884.

(30) Steinbach, P. J. Inferring lifetime distributions from kinetics by maximizing entropy using a bootstrapped model. *J. Chem. Inf. Comput. Sci.* **2002**, *42*, 1476–1478.

(31) Steinbach, P. J.; Ionescu, R.; Matthews, C. R. Analysis of kinetics using a hybrid maximum-entropy/nonlinear-least-squares method: application to protein folding. *Biophys. J.* **2002**, *82*, 2244–2255.

(32) Sottini, S.; Abbruzzetti, S.; Viappiani, C.; Ronda, L.; Mozzarelli, A. Determination of microscopic rate constants for CO binding and migration in myoglobin encapsulated in silica gels. *J. Phys. Chem. B* **2005**, *109*, 19523–19528.

(33) Bruno, S.; Faggiano, S.; Spyraakis, F.; Mozzarelli, A.; Cacciatori, E.; Dominici, P.; Grandi, E.; Abbruzzetti, S.; Viappiani, C. Different roles of protein dynamics and ligand migration in non-symbiotic hemoglobins AHb1 and AHb2 from *Arabidopsis thaliana*. *Gene* **2007**, *398*, 224–233.

(34) Abbruzzetti, S.; Grandi, E.; Bruno, S.; Faggiano, S.; Spyraakis, F.; Mozzarelli, A.; Cacciatori, E.; Dominici, P.; Viappiani, C. Ligand migration in non symbiotic hemoglobin AHb1 from *Arabidopsis thaliana*. *J. Phys. Chem. B* **2007**, *111*, 12582–12590.

(35) Abbruzzetti, S.; Spyraakis, F.; Bidon-Chanal, A.; Luque, F. J.; Viappiani, C. Ligand migration through heme protein cavities: insights from laser flash photolysis and molecular dynamics simulations. *Phys. Chem. Chem. Phys.* **2013**, *15*, 10686–10701.

(36) Case, D. A.; Babin, V.; Berryman, J. T.; Betz, R. M.; Cai, Q.; Cerutti, D. S.; Cheatham, T. E., III; Darden, T. A.; Duke, R. E.; Gohlke, H.; et al. *AMBER14*; University of California, San Francisco, 2014.

(37) Capece, L.; Boechi, L.; Perissinotti, L. L.; Arroyo-Mañez, P.; Bikiel, D. E.; Smulevich, G.; Marti, M. A.; Estrin, D. A. Small ligand-globin interactions: Reviewing lessons derived from computer simulation. *Biochim. Biophys. Acta, Proteins Proteomics* **2013**, *1834*, 1722–1738.

(38) Marti, M. A.; Capece, L.; Bidon-Chanal, A.; Crespo, A.; Guallar, V.; Luque, F. J.; Estrin, D. A. In *Methods in Enzymology*; Poole, R. K., Ed.; Academic Press, 2008; Vol. 437, pp 477–498.

(39) Nadra, A.; Marti, M. A.; Pesce, A.; Bolognesi, M.; Estrin, D. A. Exploring the molecular basis of heme coordination in human neuroglobin. *Proteins: Struct., Funct., Genet.* **2008**, *71*, 695–705.

(40) Capece, L.; Lewis-Ballester, A.; Yeh, S.-R.; Estrin, D. A.; Marti, M. A. Complete reaction mechanism of indoleamine 2,3-dioxygenase

as revealed by QM/MM simulations. *J. Phys. Chem. B* **2012**, *116*, 1401–1413.

(41) Arroyo Mañez, P.; Lu, C.; Boechi, L.; Marti, M. A.; Shepherd, M.; Wilson, J. L.; Poole, R. K.; Luque, F. J.; Yeh, S.-R.; Estrin, D. A. Role of the distal hydrogen-bonding network in regulating oxygen affinity in the truncated hemoglobin III from *Campylobacter jejuni*. *Biochemistry* **2011**, *50*, 3946–3956.

(42) Marti, M. A.; Crespo, A.; Capece, L.; Boechi, L.; Bikiel, D. E.; Scherlis, D. A.; Estrin, D. A. Dioxygen affinity in heme proteins investigated by computer simulation. *J. Inorg. Biochem.* **2006**, *100*, 761–770.

(43) Bikiel, D. E.; Boechi, L.; Capece, L.; Crespo, A.; DeBiase, P. M.; DiLella, S.; GonzálezLebrero, M. C.; Marti, M. A.; Nadra, A. D.; Perissinotti, L. L.; et al. Modeling heme proteins using atomistic simulations. *Phys. Chem. Chem. Phys.* **2006**, *8*, 5611–5628.

(44) Cohen, J.; Arkhipov, A.; Braun, R.; Schulten, K. Imaging the migration pathways for O₂, CO, NO, and Xe inside myoglobin. *Biophys. J.* **2006**, *91*, 1844–1857.

(45) Cohen, J.; Olsen, K. W.; Schulten, K. Finding gas migration pathways in proteins using implicit ligand sampling. *Methods Enzymol.* **2008**, *437*, 439–457.

(46) Forti, F.; Boechi, L.; Bikiel, D.; Marti, M. A.; Nardini, M.; Bolognesi, M.; Viappiani, C.; Estrin, D.; Luque, F. J. Ligand migration in *Methanosarcina acetivorans* protoglobin: effects of ligand binding and dimeric assembly. *J. Phys. Chem. B* **2011**, *115*, 13771–13780.

(47) Forti, F.; Boechi, L.; Estrin, D. A.; Marti, M. A. Comparing and combining implicit ligand sampling with multiple steered molecular dynamics to study ligand migration processes in heme proteins. *J. Comput. Chem.* **2011**, *32*, 2219–2231.

(48) Gabba, M.; Abbruzzetti, S.; Bruno, F. S. S.; Mozzarelli, A.; Luque, F. J.; Viappiani, C.; Cozzini, P.; Nardini, M.; Germani, F.; Bolognesi, M.; et al. CO rebinding kinetics and molecular dynamics simulations highlight dynamic regulation of internal cavities in human cytoglobin. *PLoS One* **2013**, *8*, e49770.

(49) Oliveira, A.; Singh, S.; Bidon-Chanal, A.; Forti, F.; Marti, M. A.; Boechi, L.; Estrin, D. A.; Dikshit, K. L.; Luque, F. J. Role of PheE15 gate in ligand entry and nitric oxide detoxification function of *Mycobacterium tuberculosis* truncated hemoglobin N. *PLoS One* **2012**, *7*, e49291.

(50) Boubeta, F. M.; Bari, S. E.; Estrin, D. A.; Boechi, L. Access and Binding of H₂S to Hemeproteins: The Case of HbI of *Lucina pectinata*. *J. Phys. Chem. B* **2016**, *120*, 9642–9653.

(51) Boron, I.; Bustamante, J.; Davidge, K.; Singh, S.; Bowman, L.; Tinajero-Trejo, M.; Carballal, S.; Radi, R.; Poole, R.; Dikshit, K. Ligand uptake in *Mycobacterium tuberculosis* truncated hemoglobins is controlled by both internal tunnels and active site water molecules. *F1000Research* **2015**, *4*, 22.

(52) Bustamante, J. P.; Szretter, M. E.; Sued, M.; Marti, M. A.; Estrin, D. A.; Boechi, L. A quantitative model for oxygen uptake and release in a family of heme proteins. *Bioinformatics* **2016**, *32*, 1805–1813.

(53) Issoglio, F. M.; Campolo, N.; Zeida, A.; Grune, T.; Radi, R.; Estrin, D. A.; Bartesaghi, S. Exploring the catalytic mechanism of human glutamine synthetase by computer simulations. *Biochemistry* **2016**, *55*, 5907–5916.

(54) Humphrey, W.; Dalke, A.; Schulten, K. VMD: visual molecular dynamics. *J. Mol. Graphics* **1996**, *14*, 33–38.

(55) Di Lella, S.; Marti, M. A.; Alvarez, R. M. S.; Estrin, D. A.; Ricci, J. C. D. Characterization of the Galectin-1 carbohydrate recognition domain in terms of solvent occupancy. *J. Phys. Chem. B* **2007**, *111*, 7360–7366.

(56) Gauto, D. F.; Di Lella, S.; Guardia, C. M. A.; Estrin, D. A.; Marti, M. A. Carbohydrate-binding proteins: dissecting ligand structures through solvent environment occupancy. *J. Phys. Chem. B* **2009**, *113*, 8717–8724.

(57) Abbruzzetti, S.; Allegri, A.; Bidon-Chanal, A.; Ogata, H.; Soavi, G.; Cerullo, G.; Bruno, S.; Montali, C.; Luque, F. J.; Viappiani, C. Electrostatic tuning of the ligand binding mechanism by Glu27 in nitrophorin 7. *Sci. Rep.* **2018**, *8*, 10855.

- (58) Franzen, S.; Kiger, L.; Poyart, C.; Martin, J.-L. Heme photolysis occurs by ultrafast excited state metal-to-ring charge transfer. *Biophys. J.* **2001**, *80*, 2372–2385.
- (59) Dixon, D. W.; Kirmaier, C.; Holten, D. Picosecond photodissociation of six-coordinate iron(II) porphyrins. *J. Am. Chem. Soc.* **1985**, *107*, 808–813.
- (60) Franzen, S.; Bohn, B.; Poyart, C.; Martin, J. L. Evidence for sub-picosecond heme doming in hemoglobin and myoglobin: a time-resolved resonance Raman comparison of carbonmonoxy and deoxy species. *Biochemistry* **1995**, *34*, 1224–1237.
- (61) Kholodenko, Y.; Volk, M.; Gooding, E.; Hochstrasser, R. M. Energy dissipation and relaxation processes in deoxy myoglobin after photoexcitation in the Soret region. *Chem. Phys.* **2000**, *259*, 71–87.
- (62) Lim, M.; Jackson, T. A.; Anfinrud, P. A. Femtosecond near-IR absorbance study of photoexcited myoglobin: dynamics of electronic and thermal relaxation. *J. Phys. Chem.* **1996**, *100*, 12043–12051.
- (63) Martin, J. L.; Migus, A.; Poyart, C.; Lecarpentier, Y.; Astier, R.; Antonetti, A. Femtosecond photolysis of CO-ligated protoheme and hemoproteins: appearance of deoxy species with a 350-fsec time constant. *Proc. Natl. Acad. Sci. U. S. A.* **1983**, *80*, 173–177.
- (64) Miller, R. J. D. Vibrational energy relaxation and structural dynamics of heme proteins. *Annu. Rev. Phys. Chem.* **1991**, *42*, 581–614.
- (65) Mizutani, Y.; Kitagawa, T. Direct observation of cooling of heme upon photodissociation of carbonmonoxy myoglobin. *Science* **1997**, *278*, 443–446.
- (66) Rodriguez, J.; Kirmaier, C.; Holten, D. Optical properties of metalloporphyrin excited states. *J. Am. Chem. Soc.* **1989**, *111*, 6500–6506.
- (67) Giordano, D.; Russo, R.; Ciaccio, C.; Howes, B. D.; di Prisco, G.; Marden, M. C.; Hui Bon Hoa, G.; Smulevich, G.; Coletta, M.; Verde, C. Ligand- and proton-linked conformational changes of the ferrous 2/2 hemoglobin of *Pseudoalteromonas haloplanktis* TAC125. *IUBMB Life* **2011**, *63*, 566–573.
- (68) Henry, E. R.; Jones, C. M.; Hofrichter, J.; Eaton, W. A. Can a two-state MWC allosteric model explain hemoglobin kinetics? *Biochemistry* **1997**, *36*, 6511–6528.
- (69) Ansari, A.; Jones, C. M.; Henry, E. R.; Hofrichter, J.; Eaton, W. Conformational relaxation and ligand binding in myoglobin. *Biochemistry* **1994**, *33*, 5128–5145.
- (70) Henry, E. R.; Bettati, S.; Hofrichter, J.; Eaton, W. A. A tertiary two-state allosteric model for hemoglobin. *Biophys. Chem.* **2002**, *98*, 149–164.
- (71) Abbruzzetti, S.; Tilleman, L.; Bruno, S.; Viappiani, C.; Desmet, F.; Doorslaer, S. V.; Coletta, M.; Ciaccio, C.; Ascenzi, P.; Nardini, M.; et al. Ligation tunes protein reactivity in an ancient haemoglobin: kinetic evidence for an allosteric mechanism in *Methanosarcina acetivorans* protoglobin. *PLoS One* **2012**, *7*, e33614.
- (72) Benabbas, A.; Ye, X.; Kubo, M.; Zhang, Z.; Maes, E. M.; Montfort, W. R.; Champion, P. M. Ultrafast dynamics of diatomic ligand binding to nitrophorin 4. *J. Am. Chem. Soc.* **2010**, *132*, 2811–2820.
- (73) Brunori, M.; Giuffrè, A.; Nienhaus, K.; Nienhaus, G. U.; Scandurra, F. M.; Vallone, B. Neuroglobin, nitric oxide, and oxygen: functional pathways and conformational changes. *Proc. Natl. Acad. Sci. U. S. A.* **2005**, *102*, 8483–8488.
- (74) Brunori, M. Nitric oxide moves myoglobin centre stage. *Trends Biochem. Sci.* **2001**, *26*, 209–210.
- (75) Ostermann, A.; Waschipky, R.; Parak, F. G.; Nienhaus, G. U. Ligand binding and conformational motions in myoglobin. *Nature* **2000**, *404*, 205–208.
- (76) Schotte, F.; Lim, M.; Jackson, T. A.; Smirnov, A. V.; Soman, J.; Olson, J. S.; Phillips, G. N., Jr.; Wulff, M.; Anfinrud, P. A. Watching a protein as it functions with 150-ps time-resolved X-ray crystallography. *Science* **2003**, *300*, 1944–1947.
- (77) Nienhaus, K.; Nienhaus, G. U. Ligand dynamics in heme proteins observed by Fourier transform infrared-temperature derivative spectroscopy. *Biochim. Biophys. Acta, Proteins Proteomics* **2011**, *1814*, 1030–1041.
- (78) Abbruzzetti, S.; Faggiano, S.; Bruno, S.; Spyraakis, F.; Mozzarelli, A.; Dewilde, S.; Moens, L.; Viappiani, C. Ligand migration through the internal hydrophobic cavities in human neuroglobin. *Proc. Natl. Acad. Sci. U. S. A.* **2009**, *106*, 18984–18989.
- (79) Goldbeck, R. A.; Bhaskaran, S.; Ortega, C.; Mendoza, J. L.; Olson, J. S.; Soman, J.; Kliger, D. S.; Esquerra, R. M. Water and ligand entry in myoglobin: Assessing the speed and extent of heme pocket hydration after CO photodissociation. *Proc. Natl. Acad. Sci. U. S. A.* **2006**, *103*, 1254–1259.
- (80) Goldbeck, R. A.; Pillsbury, M. L.; Jensen, R. A.; Mendoza, J. L.; Nguyen, R. L.; Olson, J. S.; Soman, J.; Kliger, D. S.; Esquerra, R. M. Optical detection of disordered water within a protein cavity. *J. Am. Chem. Soc.* **2009**, *131*, 12265–12272.
- (81) Wolfenden, R.; Snider, M. J. The depth of chemical time and the power of enzymes as catalysts. *Acc. Chem. Res.* **2001**, *34*, 938–945.
- (82) Snider, M. J.; Lazarevic, D.; Wolfenden, R. Catalysis by entropic effects: the action of cytidine deaminase on 5,6-dihydrocytidine. *Biochemistry* **2002**, *41*, 3925–3930.